EXPERIMENTAL AND NUMERICAL STUDY OF THE COMPOSITE WING STRUCTURE EMBEDDING SOLAR CELLS

Q Rouxel, Pierre-Antoine Dubos, Shahram Khazaie, S Lucas, Pascal Casari

AerospaceEurope Conference2020
BORDEAUX, FRANCE | 25 - 28 FEBRUARY 2020
CEAS Council of European Aerospace Societies
HOSTED BY : 3AF Association Aéronautique et Astronautique de France

EXPERIMENTAL AND NUMERICAL STUDY OF THE COMPOSITE WING STRUCTURE EMBEDDING SOLAR CELLS

Q. Rouxel [1,2], P.-A. Dubos [1], S. Khazaie [1], S. Lucas [2], P. Casari [1]

[1] Université de Nantes, Institut de recherche en Génie Civil et Mécanique (UMR CNRS 6183), 58, rue Michel Ange - BP 420, 44606 Saint-Nazaire Cedex, France
[2] XSun, 5, route de la Croix Moriau, 44350 Guérande, France

KEYWORDS: solar drone, solar cells, composite materials

ABSTRACT:

Reducing the CO_2 emissions is one of the major objectives in aerospace engineering. In this regard, XSun startup is developing an autonomous solar drone, SolarXOne. The latter is independent on one hand in decision with an autopilot and on the other hand in energy using solar cells and batteries. This paper aims at presenting the mechanical behavior of the solar cells and their interactions with composite structures. In our experimental tests, the wings are subjected to the maximum load that they will undergo during a typical flight. They have been instrumented with Distributed Optical Fiber Sensors (processed with LUNA ODiSI-B). The digital image correlation measurements (processed with VIC 3D) allow us to estimate the strain in the wings. Wing skin mechanical behavior is characterized by deformation measurements under loadings. These strains are replicated on tensile test specimens with and without solar cells. Comparison of strains in these specimens reveals the impact of solar cells on the structure.

1. INTRODUCTION:

Using solar energy on aeronautic industry can be a way to make this industry greener. For instance, for some particular missions such as monitoring, a solar drone could be used instead of a classical airplane. However, embedding solar cells in a flying structure raises issues about material behavior or interactions between solar cells and the structure. To increase the Unmanned Aerial Vehicle (UAV) performance such as flight time or the mass of on-board equipment, optimization of the mass of the structure is one of the main challenges. To ensure a light but resistant structure, some composite layers are used in SolarXOne's wings. In order to maximize the solar cell surface and to increase the stability in flight, the drone has a novel design with two spares of solar wings (Fig. 1).

Figure 1. The UAV SolarXOne developed by XSun

Wings of the drone embed solar cells allowing it to be autonomous in energy. Integration of thin-film solar cell on composites is a work item present in several studies with many industrial applications. Several studies show the electrical response of thin film silicon solar cells on carbon fiber reinforced epoxy composites under mechanical cyclic stress [1-2]. It has been observed that low strains (up to 0.3%) do not change electrical parameters such as short circuit current density or maximal power point, while larger strains (around 1%), cause them a drastic reduction, leading to a loss of cell efficiency and can generate major risks. Knowing the strain field on the wings is therefore of major importance for the proper performance of the cells.

In aerospace industry, wing loading tests are necessary to determine the mechanical behavior of the wing, as illustrated in Fig. 2 with the wing load test of the solar plane Solar Impulse 2 [3]. Some parameters such as load bearing capacity can be validated with this kind of test. In this study, these tests are performed on wings instrumented with an optical fiber sensor to measure strain on the spar, deflection of the wings and digital image correlation to estimate the strain in the wing skins. These experimental results are subsequently validated using a numerical finite element model.

Figure 2: Wing load test of Solar Impulse 2 [3]

2. BENCH AND INSTRUMENTED WINGS:

The wings that will be put on test in this section are made without solar cells. However, they have the same structure as the wings embedding solar cells. They are made of composite materials with a spar all along the wings. This spar is instrumented with an optical fiber sensor. The latter is based on the measurement of the Rayleigh backscatter and allows not only to measure the deformation all along the spar during the loading test but also to check its integrity between flights [4]. The optical fiber sensor is introduced during the composite manufacturing at the top and at the bottom of the spar (go and return). The sensor is processed with LUNA ODiSI-B software. For the acquisition, gauges are defined each 2.6 mm all along the optical fiber sensor to measure longitudinal strain.

On the upper surface of the wings, in-plane longitudinal and transversal strains are measured. This measurement is carried out, using digital image correlation method, on a region of interest (ROI) defined at the middle of the wing to limit the vertical deflection. This technique also provides information about strains and displacements from a speckle painted on the wing filmed with two cameras [5]. Fig. 3 outlines the experimental set-up.

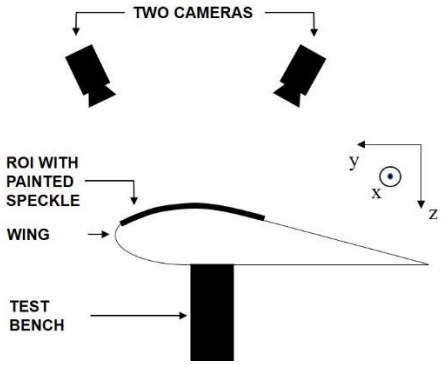

Figure 3. Two cameras filming the speckle on the wing

For each test, in addition to the measurements with optical fiber sensor and digital image correlation, the vertical deflection of the wing is measured.

The whole experiment is repeated two times on each wing in order to ensure reliable results and present a repeatability of the order of one percent.

To characterize the mechanical behavior of the wing, Euler Bernoulli theory for embedded beam and distributed load is used [6]. Considering a constant stiffness, the wing's stiffness EI_y is determined knowing the maximum deflection f_{max} (at $x = L$) via:

$$EI_y = \frac{FL^3}{8f_{max}} \quad (1)$$

in which EI_y is the flexural rigidity, F is the applied load and L is the wing's length.

Knowing the strain all along the optical fiber sensor $\varepsilon_{xx}(x)$, the curvature as a function of the x-position on the wing $\gamma(x)$ writes:

$$\gamma(x) = \frac{\varepsilon_{xx}(x)}{y} \quad (2)$$

where y is the distance to the neutral axis.

The curvature then allows to calculate the flexural rigidity $EI_y(x)$ along the wing as follows:

$$EI_y(x) = \frac{M_{fy}(x)}{\gamma(x)} \quad (3)$$

where $M_{fy}(x)$ is the moment along the wing.

To perform the loading test of the wings, a test bench is prepared and illustrated in Fig. 4. During the bench design, a particular attention has been paid to some points like uniform loading along wingspan and free upper surface of the wings for digital image correlation.

To avoid undesired free solid movements, a slider allows only a vertical translation. The position of the wing on the bench is determined by the position of the spar. The contact between the wings and the bench is made with a rubber air bladder. This ensures the continuity of the loading and a soft contact on the wings. The load is applied at the vertical, on the wing joiner.

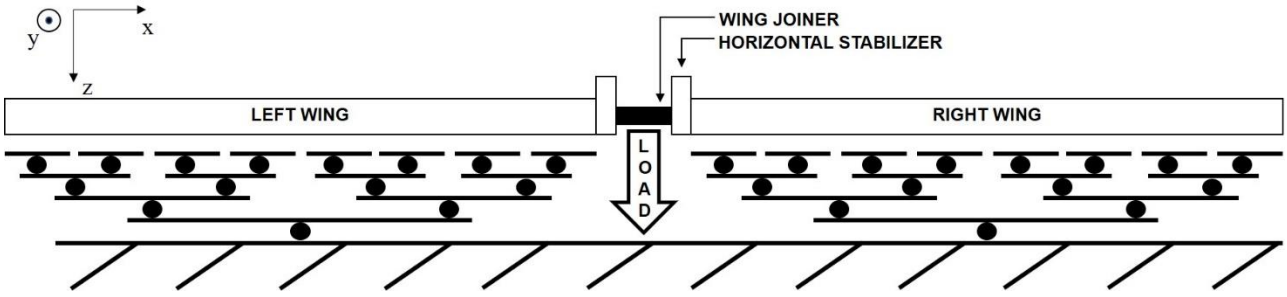

Figure 4. Scheme of the wing loading test bench

The load factor of the drone, denoted by *n,* should be defined. The latter is the ratio of the lift to the weight. It represents the overall stress on the airplane structure.

In this study, the maximum load factor seen during a typical flight is known (measured *in situ*) and the load to apply on the bench to reproduce this load factor can be expressed by the relation (4):

$$F = \left(m_{drone} - m_{wings}\right) n g k_l \qquad (4)$$

where m_{drone} is the mass of the drone, m_{wings} is the mass of the wings, g is the standard gravity and k_l is the factor of lift distribution between the front and the back wings. The mass of wings is subtracted of the drone mass because we consider inertia relief, assuming that the mass of the wing is distributed as the wing lift. Inertia relief is the fact that each element of the wing causes an inertia force in the opposite direction of any vertical acceleration [7].

3. EXPERIMENTAL TEST AND MEASUREMENTS:

Gradual loadings are applied to achieve the maximum loading. The first step is a preload applied at the wing joiner. Three loadings corresponding to 0.25, 0.5 and 0.75 of the maximum load F_{max}. The vertical wing deflection normalized by its maximum is plotted on Fig. 5, at several x-position along the wing, for these loadings.

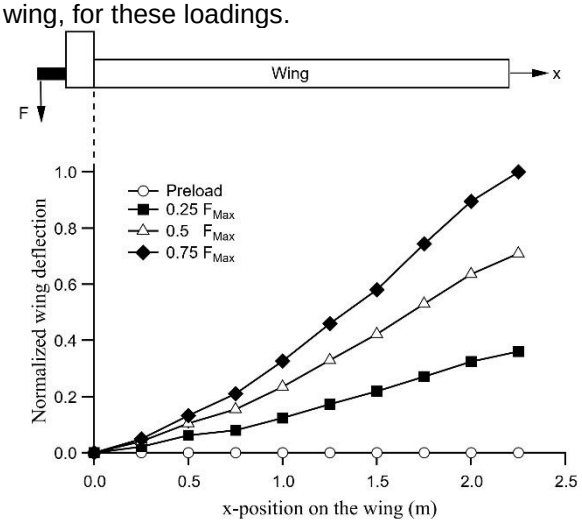

Figure 5. Wing deflection under several loadings

As expected, deflection increases with loading and with the distance of the embedding. Flexural stiffness EI_y is calculated with the maximal deflection at *x=L*, considering a constant stiffness.

The second way to obtain and validate EI_y is to measure longitudinal strain along the wing with the inserted optical fiber sensor.

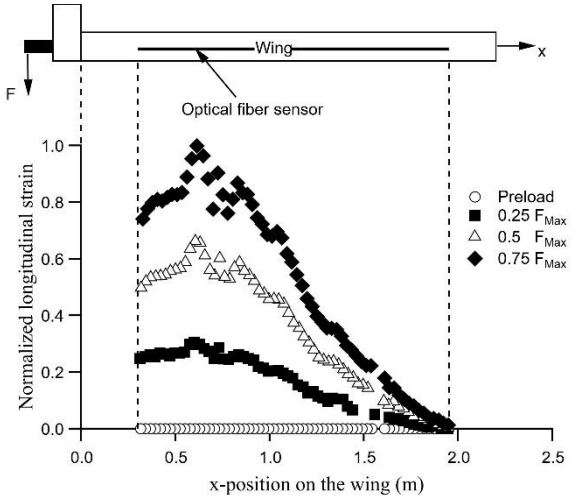

Figure 6: Strain measurement under several loadings

From Fig. 6, it can be observed that the strain in the spar is almost zero at the wing tip. Between the tip and a maximal point at *x*=0.5 m, longitudinal strain increased constantly. At this point, the spar is reinforced by the wing joiner increasing its rigidity causing lower strains to the wing's root. Variations around *x*=0.5 m might be due to the progressive integration of this reinforcement.

In-plane longitudinal e_{xx} and transversal e_{yy} strains on the external wing skin are measured under the same previous loadings.

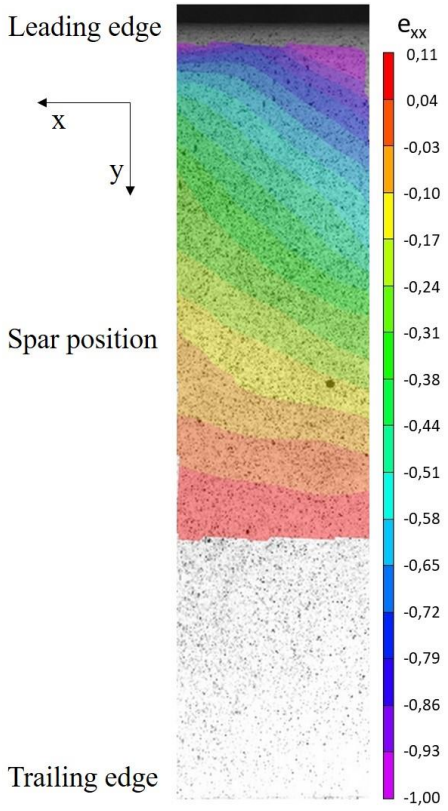

Figure 7. Normalized e_{xx} field performs with digital image correlation of a wing skin under 75% of the maximal load

Fig. 7 depicts an example of the e_{xx} field on a wing skin under 75% of the maximum load. This experimental map shows, for a constant loading (i.e. 0.75 F_{Max}) that the strain field is overall constant along the wingspan (x-direction) but strongly affected by the y-direction along the wing chord.

Along the wing chord, e_{xx} values are the quarter of e_{yy}. To analyze the variation of e_{yy} for several loadings, Fig. 8 shows these strains versus y-position in a ROI chosen at the middle of the spar. The fact that the composite stack is not a balanced as well as the wing geometry seems to be at the origin of the strong variations of e_{yy} along the chord in particular for the most important loadings

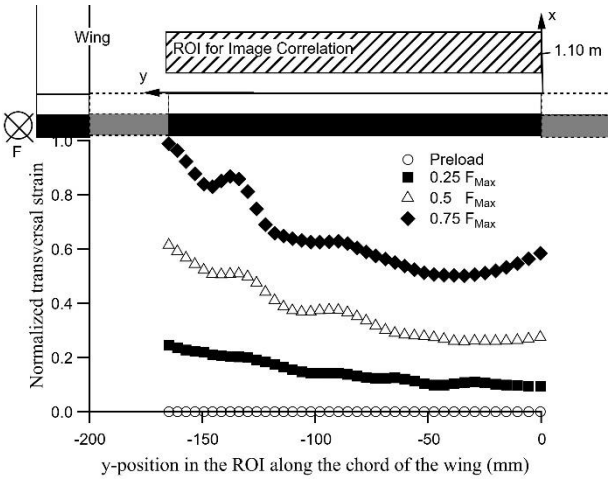

Figure 8. Transversal strain e_{yy} along the chord

For the next tests, the maximum e_{yy} observed during these previous tests will serve as a reference for tensile tests performed with specimen parts.

4. RESULTS:

4.1. Wing stiffness characterization

Once the measurements of the wing deflection are done, the stiffness of the wing is calculated using Eq. 1. This method gives a constant stiffness along the wingspan. We confront this value with those calculated from strain in the spar obtained with optical fiber sensor. This method gives a stiffness which increases near to the embedding.

On the Fig. 9, it implies that both methods give close results. Increase of rigidity for x<0.5 m is due to spar reinforcement. Unfortunately, the Euler Bernoulli beam theory is not optimum in this studied case since it is too simplistic for the application because of the presence of flaps on the wing and the fact that the chord is not very small in front of the length. A finite element model will be therefore necessary to estimate more precisely the response of each part of the wing. In the following part a focus on strain distribution on the skin of the wing under tensile tests, is given.

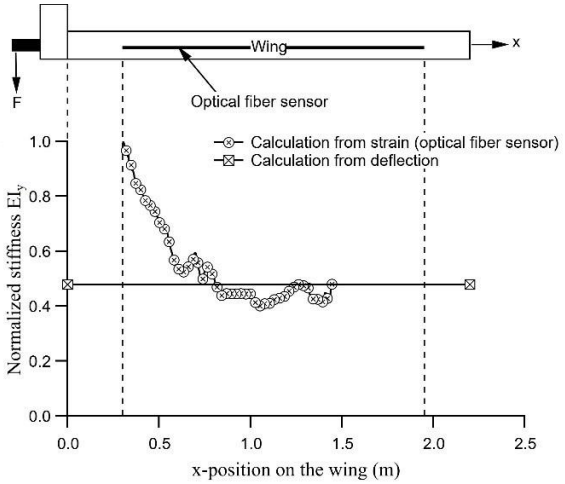

Figure 9. Wing stiffness

4.2. Wing skin study

Knowing the maximum strain in the external wing skin under the maximum loading, we reproduce this strain on specimen parts. Two specimen parts are manufactured, one with a solar cell and the second without. The composite stack is described in Tab. 1.

Material type	Orientation	Thickness [mm]
Fiberglass composite	45° / -45°	0.035 (each ply)
Adhesive	0°	0.005
Honeycomb core	W direction	1.5
Adhesive	0°	0.005
Fiberglass composite	45° / -45°	0.035 (each ply)

Table 1. Specimen parts material stack

Five loading increments are applied to approach the maximum strain. Strain is measured using the digital image correlation method.
Fig. 10 (a) shows the longitudinal strain e_{xx} field on the specimen part without solar cell. Strain is overall homogeneous according to the tensile direction.

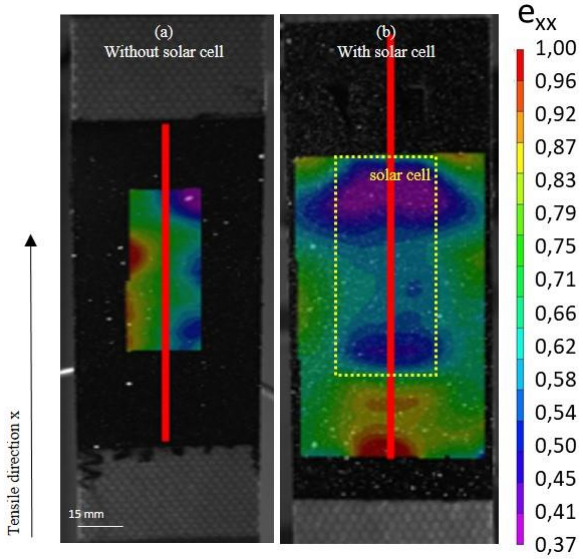

Figure 10. Normalized e_{xx} field performs with digital image correlation for specimen part without (a) and with (b) solar cell under loading of 400 N

Fig. 10 (b) shows e_{xx} on the specimen part with solar cell. Two strain levels are observed: in the solar cell area (yellow rectangle) and outside this area.

Comparing e_{xx} along the red line in the measured ROI for both specimen parts (Fig 12 (a) and (b)), a lower strain on the solar cell area (x between x=50 mm and x=100 mm) is clearly observed. This result characterizes the stiffness increasing of the composite material by the solar cell. Higher strain is measured out of the solar cell area for the specimen part with solar cell. For all loading increments the same strain profile is measured. These experimental results are verified using a finite element model on Abaqus. For this purpose, a cantilever beam model with the same geometry as defined earlier is numerically constructed to which the pressure load is applied to the whole surface at $x = L$. We will consider two numerical cases with and without the presence of the solar cell. The Material properties are summarized in Tab. 2.

	E_1 [MPa]	E_2 [MPa]	ν_{12} [-]
Fiberglass composite	26000	4450	0.29
Adhesive	55000	55000	0.3
Solar cell	106000	106000	0.3

	E_1 [MPa]	G_{12} [MPa]	ν_{12} [-]
Honeycomb core	138	24	0.28

Table 2. Material properties used in the numerical model

The finite element mesh is composed of linear hexahedral elements. The cell and the wing contain $20 \times 9 \times 1$ and $120 \times 12 \times N_z$ elements respectively wherein N_z is 1 for each ply.

The e_{xx} fields with and without the solar cell are shown in Fig. 11.

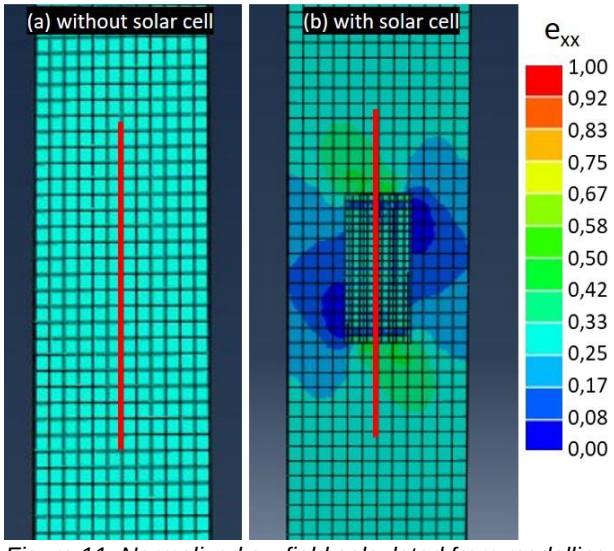

Figure 11. Normalized e_{xx} field calculated from modelling of specimen part without (a) and with (b) solar cell for a 400 N load

A comparison with Fig. 10 reveals that the experimental variation of the strain field is appropriately reproduced through our numerical model. Fig. 12 shows a comparison of the experimental and numerical normalized strain fields following the red line defined earlier. Even though the numerical and experimental results are different, they have a similar pattern within the solar cell (the yellow area as indicated in Fig 12). Furthermore, the difference in the values is a result of the material properties used in our numerical models (Tab. 2) which are taken from the literature and not by doing the material characterization tests. It is worth noting the strain concentration in a region close to the edges of the cell.

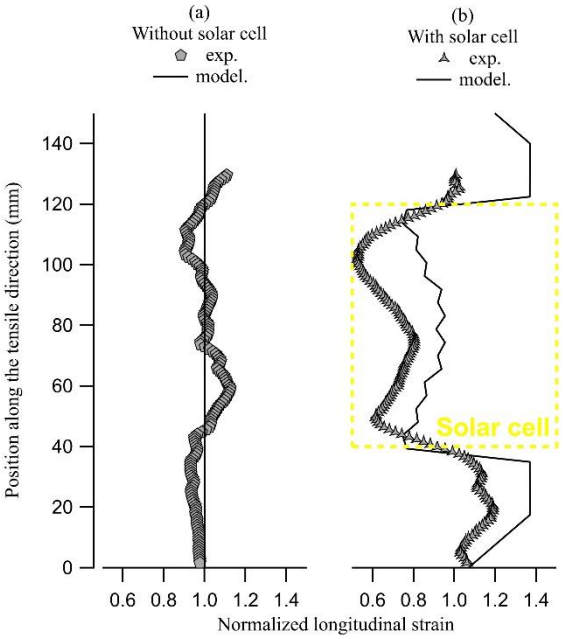

Figure 12. Normalized longitudinal strain e_{xx} along specimen parts under 400 N during tensile test: experimentation and modelling

5. CONCLUSION:

In this study, a wing loading test with innovative instrumentation was presented with measurements of strain in the spar and the wing deflection under loadings. Flexural rigidity of the wing is calculated with these values. Strains on the extrados wing skin are also measured. Knowledge of the higher strain on the composite materials allows to begin a campaign of characterization of the solar cell effect on the composite materials. In future works, fatigue tests with composite parts embedding solar cells will be carried out.

6. REFERENCE:

1. Jason Maung, K. Thomas Hahn, K. & Ju, Y.S. (2010). Multifunctional integration of thin-film silicon solar cells on carbon-fiber-reinforced epoxy composites. *Solar Energy.* 84. 450-458.

2. Yossef, M. & Chen, A. (2016). Strain Effect on the Performance of Solar Cells. *Earth and Space*. 869-880.

3. Fields, H. (2014). The solar-Powered Plane That'll Fly Around the World. *Discover*. June 2014.

4. Samiec, D. (2012). Distributed fibre-optic temperature and strain measurement with extremely high spatial resolution. *Photonik international.* 10-13.

5.Alila, F. Fajoui, J. Kchaou, M. Casari, P. Wali, N. & Gerard, R. (2016). Mechanical characterization of sandwich composite structure using a new experimental approach. *Advanced Composites Letters*. Vol. 25. 117-120.

6.Thorin, A. & Forêt, G. (2014). *Calcul des structures*. 12-32.

7.Light Aircraft Association, (2008). *Aircraft Loads and Load Testing*. 1-3.